STRATIGRAPHIC AND STRUCTURAL FRAMEWORK OF THE CLEMENTE-TOMAS AND CORSAIR GROWTH FAULT SYSTEMS IN THE TEXAS CONTINENTAL SHELF

Olabisi Ajiboye and Seiichi Nagihara

Department of Geosciences, Texas Tech University, MS 1053, Lubbock, Texas 79409–1053, U.S.A.

ABSTRACT

The Clemente-Tomas and Corsair growth fault systems in the Texas continental shelf run roughly parallel to the shoreline. The structural development and sedimentation history of some parts of these fault systems have not been investigated in detail. The present study attempts to characterize the sedimentary structure and stratigraphy in one of those parts; an 867 mi^2 (2245 km^2) section within the Mustang Island federal lease area. A 3D seismic volume, well logs from 36 boreholes, velocity survey data from 26 wells and paleontological data from 16 wells were interpreted for this investigation. Integration of these datasets enabled us to identify 6 chronostratigraphic horizons in the Miocene and Pliocene.

Structure maps and sedimentary isopach maps were generated from them. Additional time constraints in deeper sediments were examined on seismic sections.

Based on the observations from our study area and comparison with those from previous studies on other segments of the Clemente-Tomas and Corsair fault systems, we infer two stages of structural evolution in these fault systems. The first is the active growth faulting period in the early to middle Miocene when the basic framework of the two fault systems was set. The older Clemente-Tomas growth fault was initiated by basinward evacuation of a shale mobile substrate in the late Oligocene through the early Miocene. A part of the evacuated shale body developed into a diapiric ridge. Further downslope evacuation of the shale substrate lead to mobilization of the sediments overlying the basinward flank of the shale ridge, and resulted in the primary Corsair fault. This ridge is probably equivalent to the Brazos Ridge that trends along the two fault systems in the northeast Texas shelf. There is much similarity in the basic structural framework involving the two growth fault systems between the present study area and the northeast Texas shelf. The second stage is the period of relative quiescence that followed. By the middle to late Miocene, movement of both growth fault systems slowed down considerably, as sedimentation had slowed down. Diapiric movement of the shale ridges still took place episodically and resulted in formation of graben faults in younger sediments. The last major movement of the Corsair system occurred in the Pliocene, while Clemente-Tomas system has been inactive for a longer period.

INTRODUCTION

The regional geologic framework of the Texas continental shelf is characterized by fast sedimentation, which occurred through the Cenozoic, and growth faulting (Fig. 1). Growth faults are listric normal faults that move contemporaneously with sediment deposition (Fig. 2). Shale or salt diapirism is often associated with the growth faults in the Texas continental shelf. Previous studies (e.g., Watkins et al., 1996a) have grouped these growth faults into 'fault systems' or 'fault families.' Each fault family consists of a group of faults that converge to a common detachment surface at depth. Within a fault family, there are primary (or master) and secondary faults. There are also antithetic and synthetic faults which form in association with the extension and rotation of strata as faulting occurs. While synthetic faults slide in the same direction as the associated master growth fault, antithetic faults slide in the opposite direction (Fig. 2).

Several growth fault systems exist in the Texas coastal plain and continental shelf (Fig. 1). From the inner coastal plain (oldest) to the outer shelf (youngest), they are the Wilcox (late
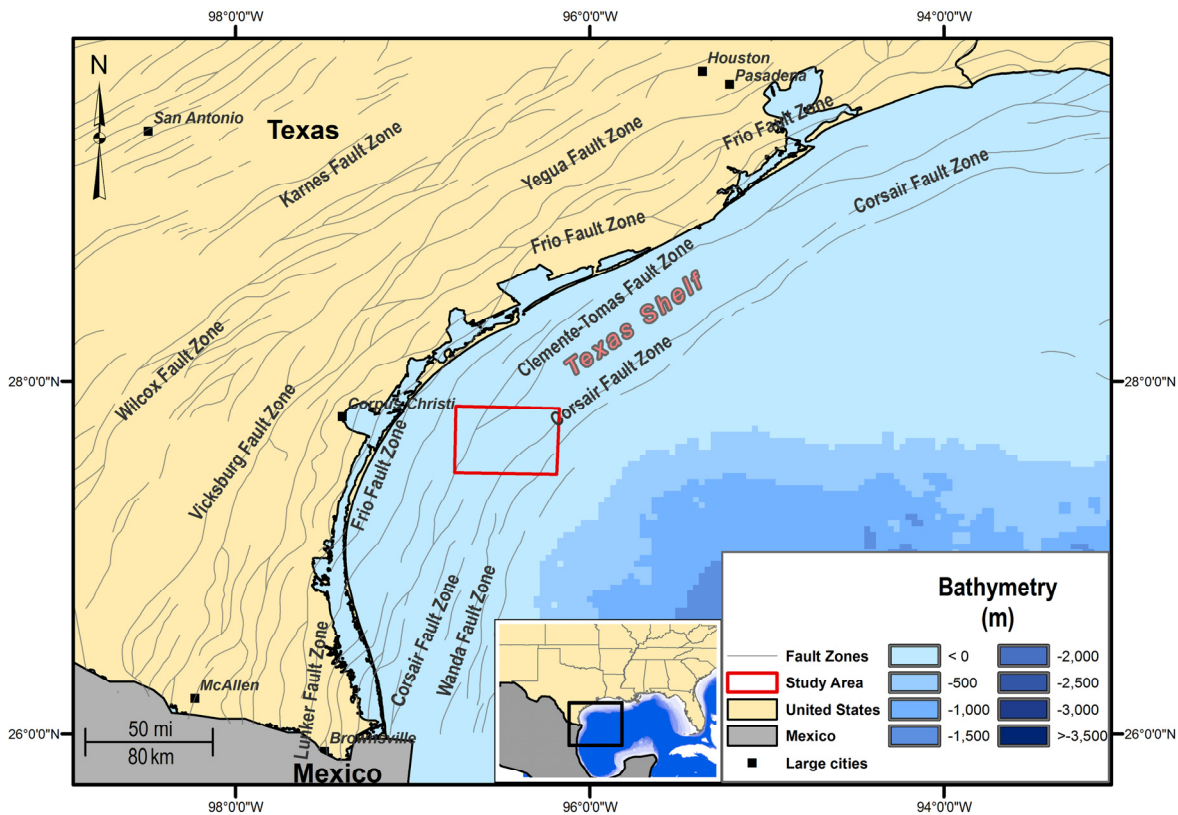
Figure 1. Map of the northwest Gulf of Mexico basin which includes the Texas continental shelf. The Wilcox, Vicksburg, Yegua, and Frio fault zones are seen trending subparallel to the shore while the Lunker, Clemente-Tomas, Corsair and Wanda growth faults trend subparallel to the shelf margin (Ewing and Lopez, 1991). The study area (red box) represents the coverage for all the surface maps used in this report.

Paleocene to early Eocene), Yegua (late Eocene), Vicksburg (early Oligocene), Frio (late Oligocene), Lunker (late Oligocene to early Miocene), Clemente-Tomas (late Oligocene to early Miocene), Corsair (middle to late Miocene), and Wanda (middle to late Miocene) growth fault systems (Ewing, 1983, 1991; Galloway et al., 1991; Stanley, 1970; Kasande, 1995).

Some growth faults in the Texas coastal plain have been associated with geothermal reservoirs (Bebout and Gutierrez, 1981; McKenna, 1997; McKenna and Sharp, 1997; Blackwell and Richards, 2004; Griggs, 2005; Nagihara and Smith, 2008; Nagihara, 2010). Most notably, sediments along the Wilcox fault zone have higher thermal gradient values than those off the fault zone. Hydrologic studies suggested that some of these faults serve as upward migration paths for fluids expelled from deep over-pressured sediments (McKenna and Sharp, 1997). In the Texas continental shelf, particularly offshore Corpus Christi, high thermal gradients (0.022°F/ft [0.04 K/m]) have been reported (Nagihara and Smith 2008; Nagihara, 2010). Temperatures of deep (>~1.8 mi [3km]) sediments along the Corsair growth fault zone are higher relative to those off the fault zone. Taylor and Land (1996) suggest, based on their reservoir fluid chemistry analyses, that pore fluids expelled from the deep Mesozoic sediments migrated upwards into Miocene sediments of the Corsair fault system. These observations indicate that the hydrologic regime of the Corsair fault system is similar to that in the Wilcox fault zone.

The primary objective of this study is to characterize in detail the stratigraphic and structural framework of Corsair and nearby Clemente-Tomas growth fault systems in the Texas shelf

in detail. It is hoped that future researchers can use the information in further investigating the geothermal and hydrologic regimes of the Texas shelf.

METHOD OF MAPPING THE SUBSURFACE STRUCTURE AND STRATIGRAPHY

The dataset used for this study consist of a time migrated 3D seismic volume that covers 867mi^2 (2245 km^2) of the Mustang Island federal lease area, provided courtesy of WesternGeco, a Schlumberger subsidiary (Figs. 1 and 3A), digital wire-line log data from 36 wells, scanned raster images of wire-line logs from 30 additional wells, core paleontologic reports for 16 wells and check shot velocity survey data for 26 wells. The well locations and distribution of data are shown in Figure 3A.

Previous studies (Morton et al., 1985, 1988; Huh, 1996; Kasande, 1995) have identified six major biostratigraphic markers in the Texas-Louisiana continental shelf. They are: *Buliminella* 1 (lower Pliocene, 3.8 Ma), *Bigenerina ascensionensis* (upper Miocene, 8 Ma), *Discorbis* 12 (upper Miocene, 9.11 Ma), *Bigenerina humblei* (middle Miocene, 13.4 Ma), *Robulus* L (lower middle Miocene, 16.3Ma), and *Marginulina ascensionensis* (lower Miocene, 18Ma). Occurrences of these fossils have been reported for 16 of the wells in the study area (Fig. 3A). The markers correspond to the last appearance datum (LADs) of each benthic foraminiferal fossil. Each benthic fossil biostratigraphic marker is associated with a regional marine transgression that impacted Miocene to Pliocene deposition on the Texas shelf (Witrock et al. 2003). By correlating each fossil using wireline
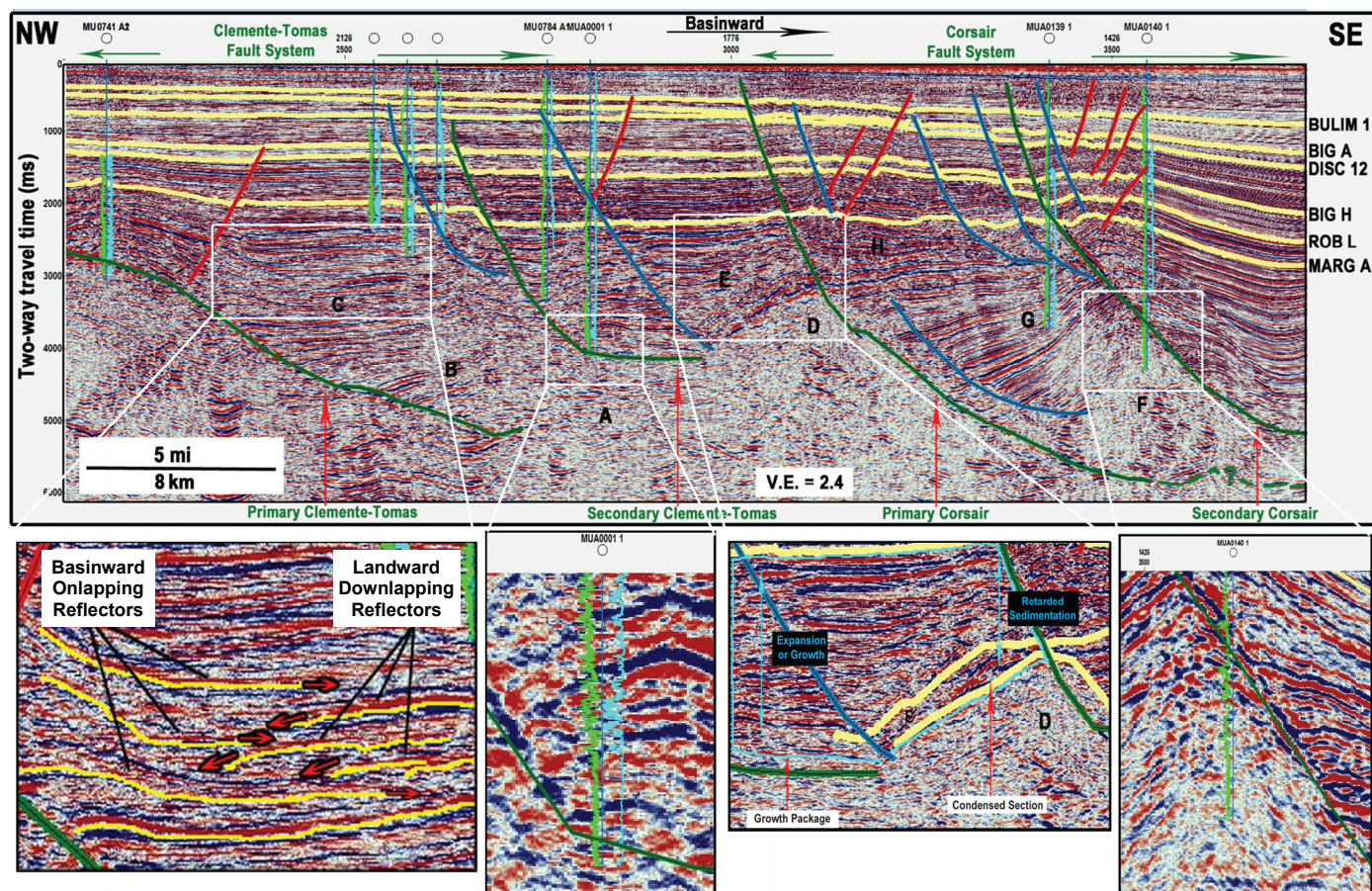
Figure 2. A northwest to southeast seismic section showing growth (green), synthetic (blue) and antithetic (red) faults in the Clemente-Tomas and Corsair fault systems. Six chronostratigraphc horizons (yellow lines) labeled as BULIM 1 (*Buliminella* 1), BIG A (*Bigenerina ascensionensis*), DISC 12 (*Discorbis* 12), BIG H (*Bigenerina humblei*), ROB L (*Robulus* L), and MARG A (*Marginulina ascensionensis*), interpreted from the wells in the Texas shelf are also shown. The labels A though H denote the sedimentary packages referenced in the text. Insets show enlargement of specific zones for clarity. The leftmost also includes our interpretation of the downlapping we describe for package 'C' in the text. We were not given permission by Schlumberger to publish the exact location of the seismic line.

lithology logs, we defined chronostratigraphic surfaces corresponding with the six biostratigraphic markers in the study area. We also identified additional chronostratigraphic surfaces based on previous studies.

We established chronostratigraphic surfaces associated with the six fossils in three major steps. First, we tied the occurrence of each fossil to lithology logs (gamma ray and/or spontaneous potential) in wells with biostratigraphic data. Second, we correlated the logs between wells with biostratigraphic data and then tied in those without biostratigraphic data (Fig. 3B). Third, we establish ties between the logs and seismic horizons (Fig. 2).

Using gamma ray and spontaneous potential logs, we differentiate shale- or mud-rich units from sandy units with shale baselines. We set 75 API and 60 mV for gamma ray and spontaneous potential, respectively, as the baseline for shale. They are the average for the log responses for the sand-shale transition zones identified in our study area. The use of a defined value for the shale base-line across the wells aids our estimation of the landward-seaward variation in sedimentary facies. In Figure 3B, the yellow shades on the gamma ray logs indicate sand-rich intervals which significantly decrease basinward. Marine transgressions often lead to the deposition of laterally extensive shale or mud separating genetically related depositional packages that we iden-

tified in the well logs. The top of such a shale unit that is closest to the depth of a fossil marker is interpreted as the corresponding biostratigraphic marker.

Before we can establish ties between the logs and the seismic volume, we must know the relationship between the two-way travel time (TWTT) and the depth. We have check-shot survey data (Fig. 3C) for 26 of the wells (Fig. 3A). The number of shot points recorded from each of these wells range from 30 to 145 check-shot points. Also, we have generated synthetic seismograms for 8 additional wells (Fig. 3A). In generating the synthetic seismograms, we first calculate the acoustic impedances of the rock layers by multiplying the P-wave velocities and densities obtained from logs. Then, reflection coefficients of the rock interfaces are obtained from the impedance contrasts (Sheriff and Geldhart, 1995). Next, the reflection coefficients are convolved with a Ricker, Klauder, or Butterworth wavelet filter to generate the synthetic seismograms. The filter that closely mirrors the seismic traces recorded through the rocks is used. Lastly, we calibrated the depth-TWTT relationship, first with the check-shot data and then by matching the synthetic seismogram with acquired seismic traces. The depth-TWTT relationships (Fig. 3C) obtained for the 34 wells are interpolated for other well locations using the Inverse Distance method (Weber and Englund, 1994).

A

B
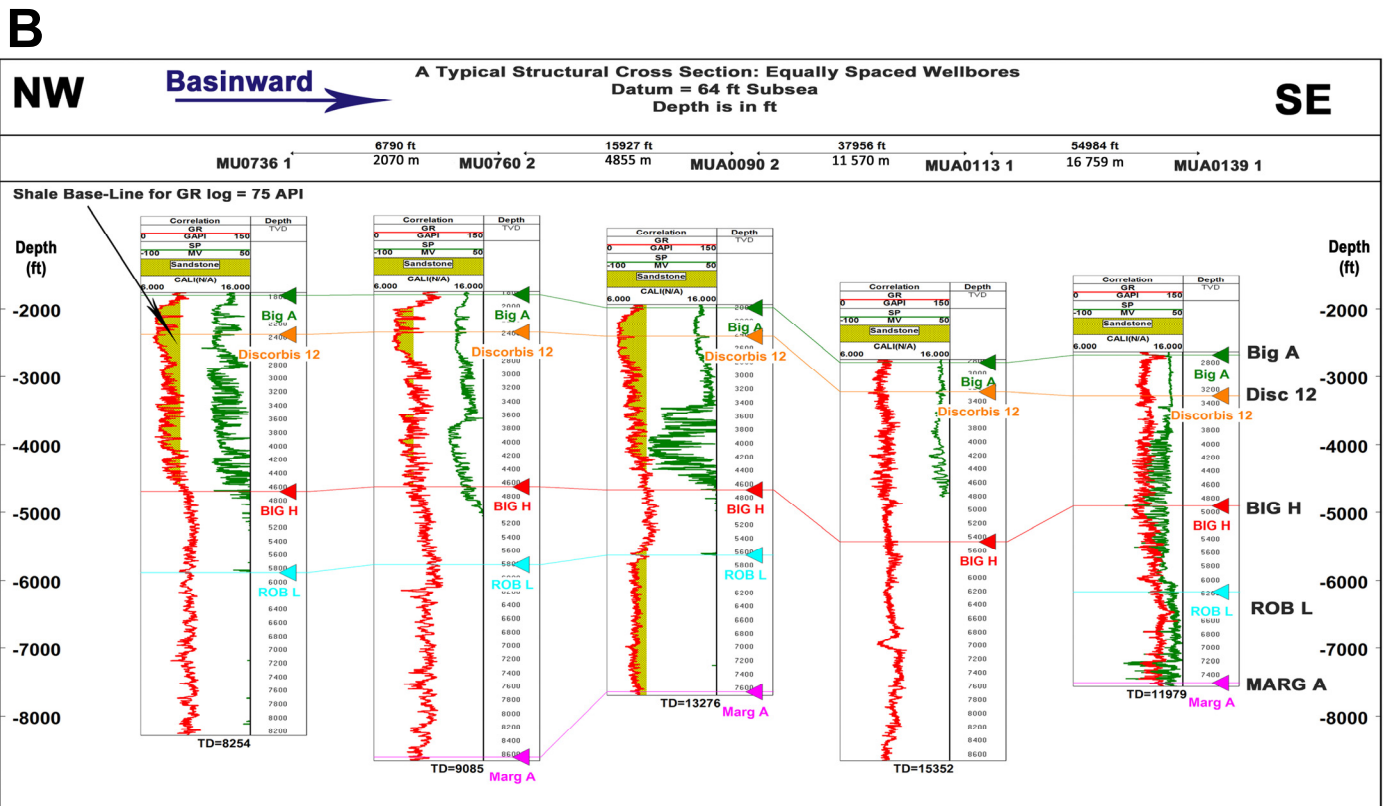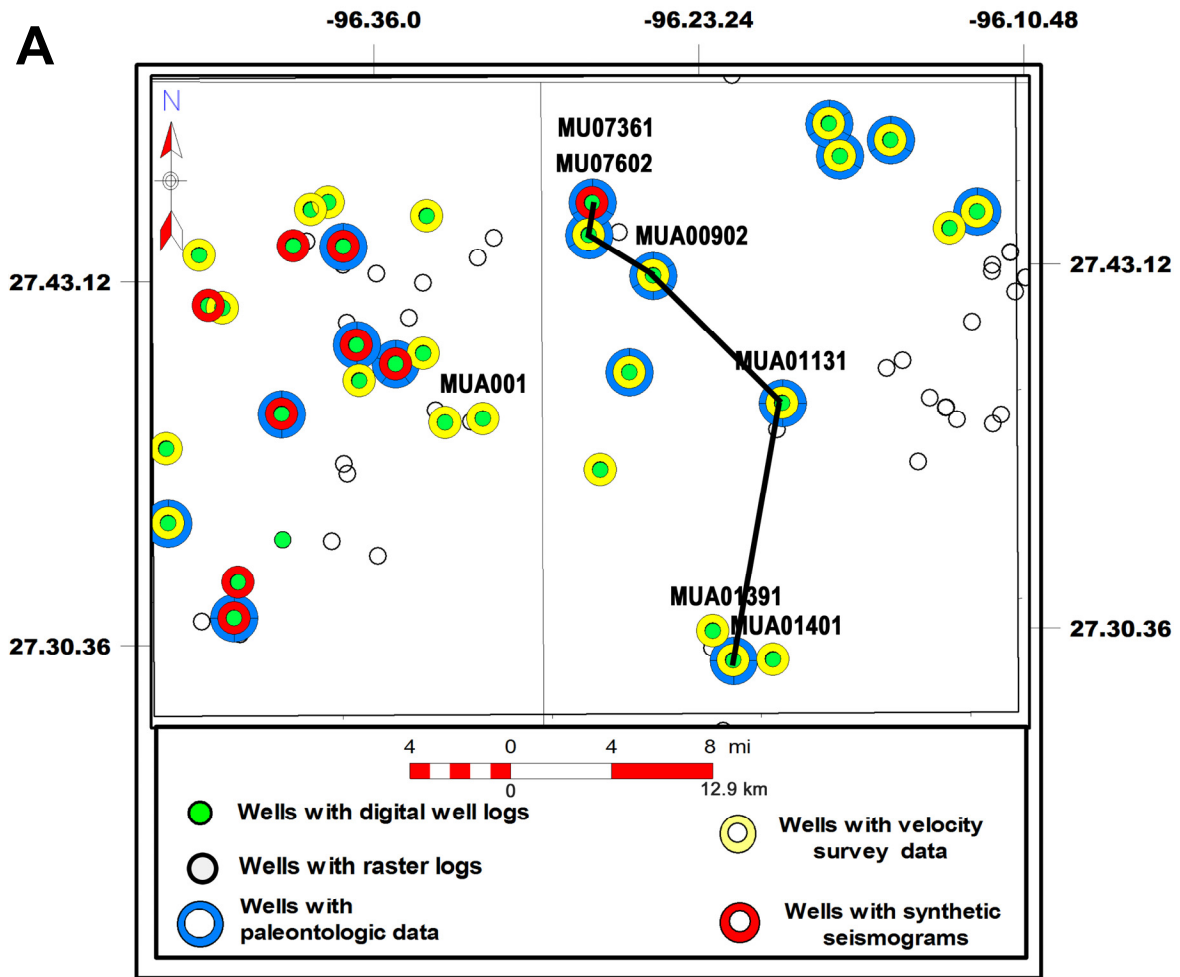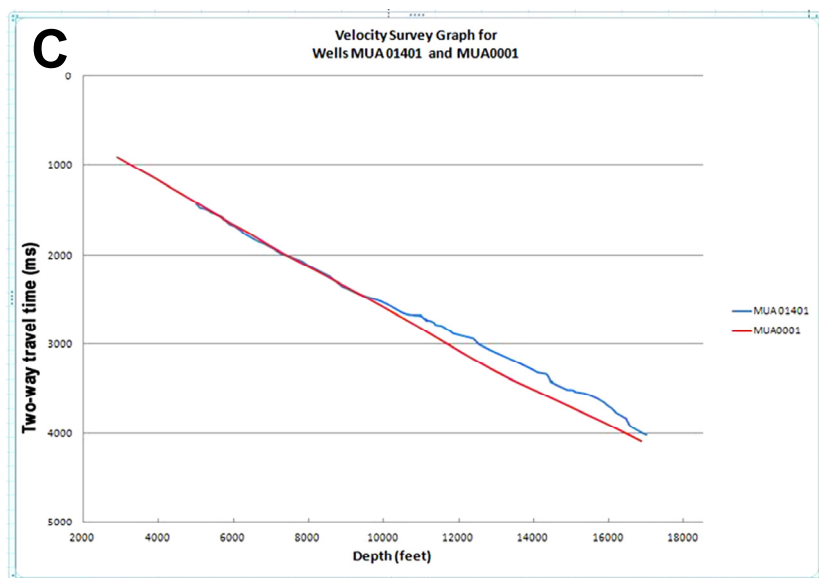
Figure 3. Description of the well data used in this study. (A—top, facing page) A map of the wells from which the log and fossil data were obtained. For each well represented by a cirlce, its color shows what type of data were made available for this study. The wells that yielded more than one set of data have multiple rings. See the legend for detail. (B—bottom, facing page) Correlation chart for the wells connected with the solid black line in top diagram. (C—left) A graph of two-wav travel time (msec) versus depth (ft) for two of the 26 wells where check-shot survey data were available. See **Figure 3A** for locations.

Knowledge of the depth-TWTT relationships (Fig. 3C) enables direct comparison between the well logs, biostratigraphic markers, and the 3D seismic volume (Fig. 2). A strong reflector that occurs at each of the 6 previously identified chronostratigraphic surfaces is picked as the relative chronostratigraphic horizon and then interpreted along a number of seismic cross-sections (Fig. 2). In identifying these horizons, we also examine reflection polarities, continuity, termination points, and seismic facies, especially in areas with sparse well coverage. A horizon identified in one cross-section is picked up in intersecting cross-sections based on its TWTT. We apply quality control to our seismic interpretations by checking loop closure; a particular horizon identified in one crossing point should eventually trace back to the same depth (TWTT) at the starting point. After seismic horizons have been identified along each of the seismic lines, they are interpolated using the Minimum Curvature method to yield a continuous surface (Fig. 4). We prefer the minimum curvature over other interpolation methods because it generates the smoothest possible surface while attempting to honor the data as closely as possible (Lam, 1983). From our seismic interpretation, we generated a series of maps showing the depths to the 6 chronologic horizons: *Buliminella* 1 (3.8 Ma), *Bigenerina ascensionensis* (8Ma), *Discorbis* 12 (9.11 Ma), *Bigenerina humblei* (13.4 Ma), *Robulus* L (16.3 Ma), and *Marginulina ascensionensis* (18Ma). These maps are shown in Figure 4. For *Buliminella* 1, we show a map of TWTTs rather than depths, because the depth of the corresponding horizons were not well constrained in the check-shot surveys.

Sediment isopach maps (Fig. 5) can be derived from these depth maps. Here, an isopach map shows the true stratigraphic thickness of sediments that deposited between two chronostratigraphic markers. To create an isopach map, we calculate the perpendicular distance to the dip of a younger chronostratigraphic surface from an older surface (Groshong, 2006). Four isopach maps (Fig. 5) are created; *Marginulina* A – *Robulus* L (lower to lower middle Miocene), *Robulus* L – *Bigenerina* H (lower middle to middle Miocene), *Bigenerina* H – *Discorbis* 12 (middle to upper middle Miocene), and *Discorbis* 12 – *Bigenerina* A (upper Miocene). For each of the isopachs, by dividing the sediment thickness by the time, we obtain an estimate for the sedimentation rate (Table 1). Readers should note

that these estimates do not account for sediment compaction, and thus, are probably lower than the true sedimentation rates at the time of the deposition.

Faults (Fig. 2) are identified on the seismic sections based on observations of discontinuity in reflection horizons and their geometry. Most of the faults in the study area run roughly parallel to the shorelines (Fig. 1). Therefore, we primarily use seismic sections in the dip direction (NW–SE) of the continental shelf in identifying faults and other sedimentary structures (Fig. 2). A fault plane can be delineated by offsets existing between the termination points of horizons in the same vicinity. The aforementioned depth and isopach maps (Figs. 4 and 5) show the traces of the faults (the lines along which fault planes intersect stratigraphic/time horizons and sediment thicknesses respectively).

OBSERVATIONS

The Clemente-Tomas Growth Fault System

Four lines of evidence suggest that the Clemente-Tomas growth faults detach and truncate in mobile substrates made predominantly of shale rather than salt. First, relatively high gamma ray and spontaneous potential log readings are found in the toe region of the faults, below the décollement of the secondary listric fault ('A' in Figures 2 and 6A). Second, the seismic P-wave velocities (8200 ft/sec or 2500 m/sec; Fig. 3C) of sediments in the same vicinity are much slower than those of rock salt (~15,000 ft/sec or ~4575 m/sec; Sheriff and Geldhart, 1995). Third, reflections along the presumed detachment surfaces are of low amplitude in general and cannot be clearly defined in many places (Figs. 2 and 6A). This is more typical for a shale detachment surface across which there is little seismic impedance contrast. If it is a salt detachment or a salt weld, its reflections would be strong and discrete (McDonnell et al., 2009). Fourth, the secondary Clemente-Tomas faults terminate at the flank of a broad, deeply buried anticline ('D' in Figures 2 and 6B), and this anticline has appearance similar to that of the shale ridge found in another section of the Clemente-Tomas system to the northeast of our study area (the so-called 'Brazos Ridge;' Bradshaw and Watkins, 1994; Watkins et al., 1996). The top of this anticline is defined by weak reflections, unlike the top of a salt body. Within the anticline, reflections are rather chaotic, and they do not show
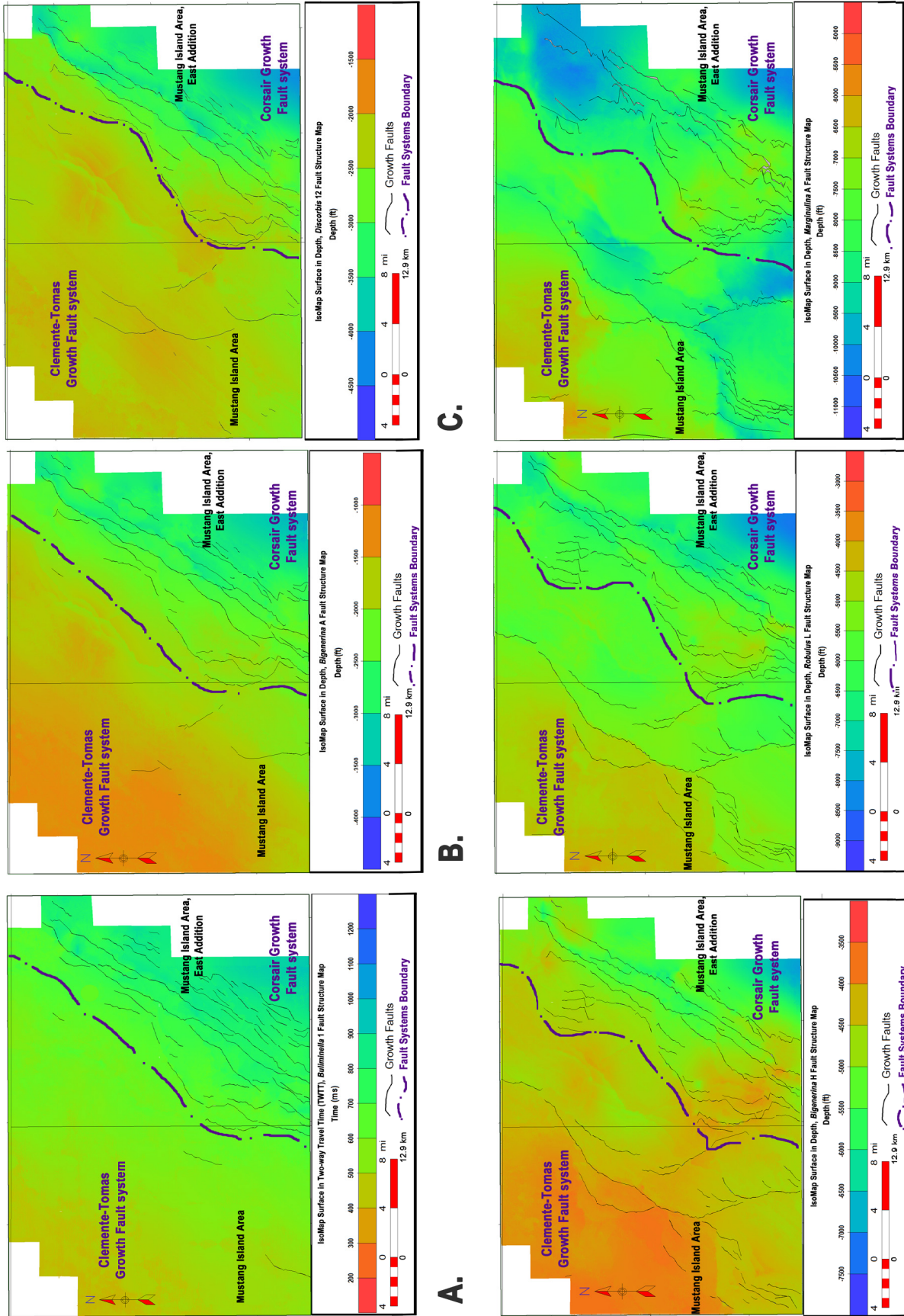
Figure 4. Time-structure map for (A) *Buliminella 1* and depth-structure maps for (B) *Bigenerina ascensionensis*, (C) *Discorbis 12*, (D) *Bigenerina humblei*, (E) *Robulus L*, and (F) *Marginulina ascensionensis* chronostratigraphic surfaces. For each map, depths to the chronostratigraphic surface are color-coded with red being the shallowest and blue being the deepest. Fault traces are drawn as blue lines.
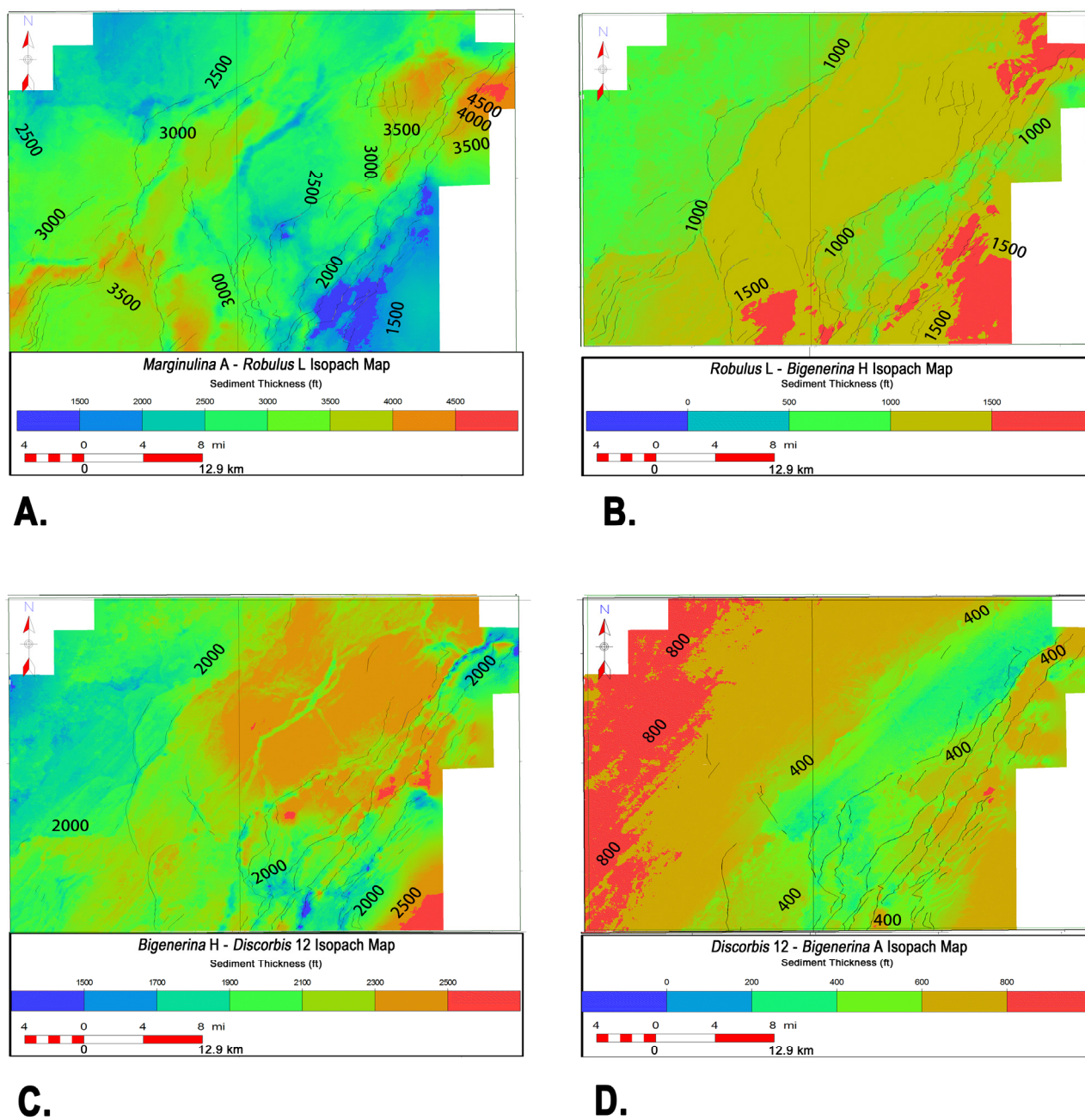
Figure 5. A series of maps showing interval sediment thickness between the chronostratigraphic surfaces identified in this study. The sediment thicknesses are isopachs measured perpendicular to the dip of the beds. **(A)** *Marginulina* A – *Robulus* L, **(B)** *Robulus* L – *Bigenerina* H, **(C)** *Bigenerina* H – *Discorbis* 12, and **(D)** *Discorbis* 12 – *Bigenerina* A horizons. Sediment thicknesses are color-coded with red being the thickest and blue being the thinnest.

Table 1. Table showing isopach intervals and their geologic and depositional series, sediment thicknesses, and sedimentation rates. There was high sedimentation in the lower to lower middle Miocene and it decreased by middle to upper Miocene.

Isopach Interval	Geologic Series	Depositional Period (m.y.)	Range of Sediment Thicknesses (ft)	Range of Sedimentation Rates (ft/m.y.)
Marginulina A – *Robulus* L	lower to lower middle Miocene	1.7	1500 – 4500	882 – 2647
Robulus L – *Bigenerina* H	lower middle to upper middle Miocene	2.9	500 – 1500	172 – 517
Bigenerina H – *Discorbis* 12	upper middle to upper Miocene	4.3	1500 – 2500	349 – 581
Discorbis 12 – *Bigenerina* A	within upper Miocene	1.1	200 – 800	182 – 727
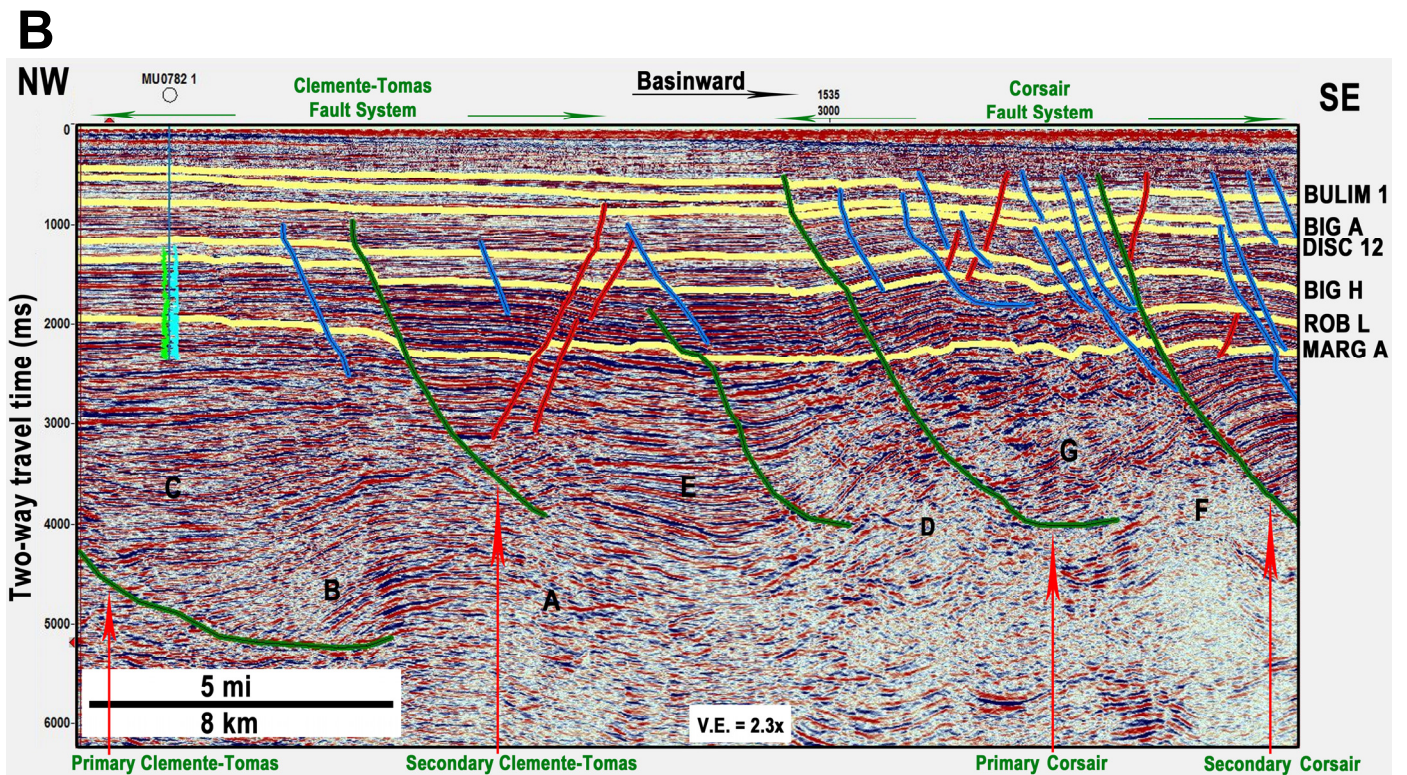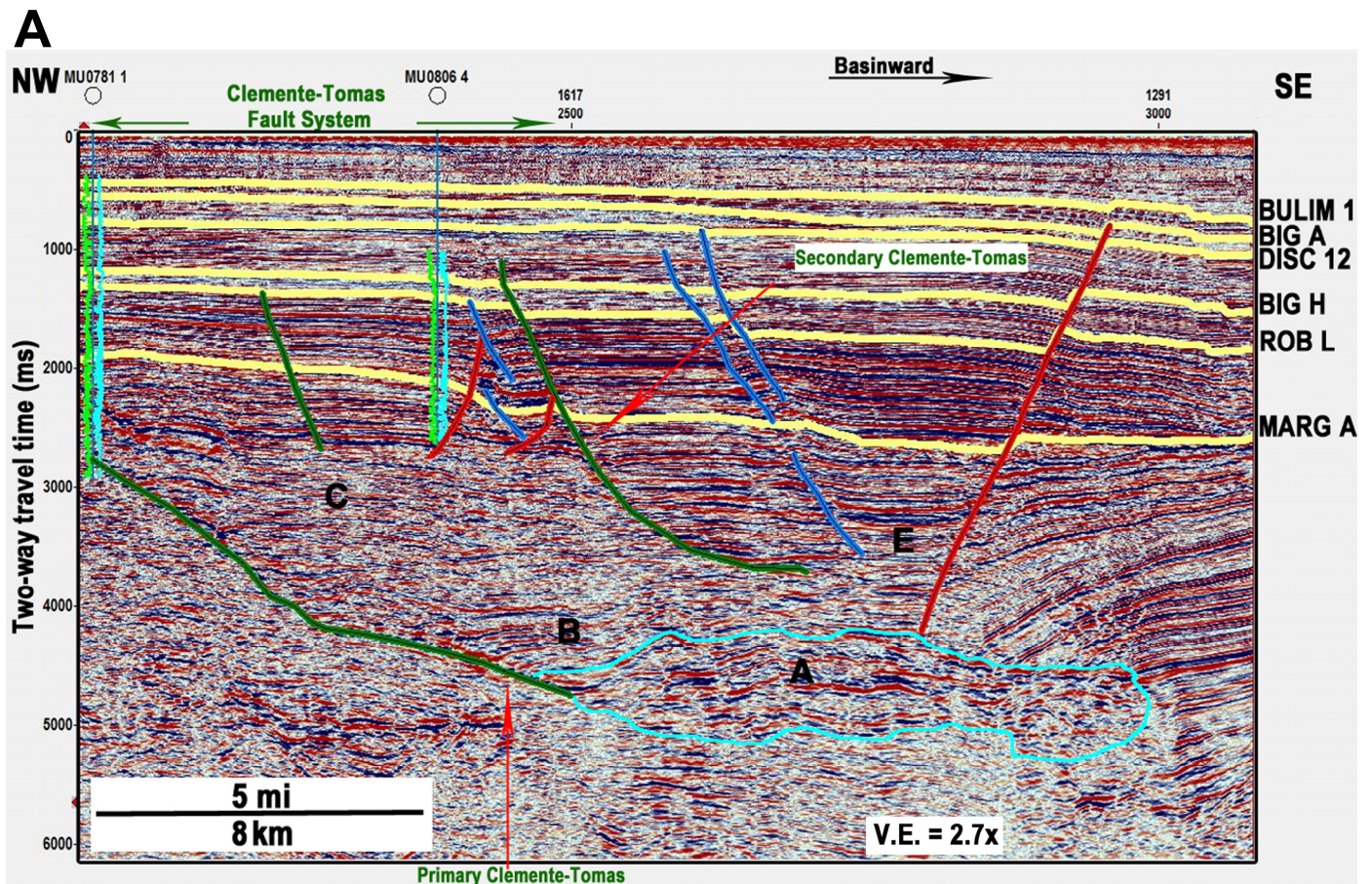
Figure 6. Northwest-southeast (basinward-dipping) seismic sections: (A) This section runs parallel to the section in **Figure 2** and located approximately 7 mi away to the southwest along the strike of the fault systems. (B) This section is located between **Figures 2** and **6A**. Labeling of the sediment packages is consistent between the three seismic sections. We were not given permission by Schlumberger to publish the exact locations of the seismic lines.

any obvious indication of velocity pull-up typical of a salt structure.

Depending on the position along the Clemente-Tomas system, another, smaller, antiform body ('A' in Figures 2 and 6A) can be seen immediately landward from the presumed shale ridge ('D' in Figures 2 and 6B). The primary fault of the system detaches to this body. Generally concave-downward, sub-parallel reflections are seen within this body. As previously mentioned, based on the gamma-ray and sonic log responses within this sedimentary unit, we believe that it is another body of shale. This feature is more clearly distinguishable in the southwestern section of the fault system within our study area (Fig. 6A) than in the northeastern section along the strike (Fig. 6B).

Overlying this antiform shale body on the hanging wall of the primary Clemente-Tomas growth fault is another series of sub-parallel reflections (labeled 'B' in Figure 2). Dip of these strata varies along the strike of the fault system. In the southwest, it is near horizontal (Fig. 6A). In the northeast, it dips landward with an average slope of 3° (Fig. 6B). Overlying package B is another set of sub-parallel reflections ('C' in Figures 2 and 6A). Reflections within this unit are rather obscure compared with its surroundings. They dip gently basinward, while showing concave-upward curvature. This gives an appearance of a syncline except that the reflections are not continuous across this package.

A series of strata lie conformably over the landward flank of the presumed shale ridge ('D' in Figures 2 and 6). In some parts along the fault system, they also lie conformably over the basinward flank of the other antiform salt body 'A.' This sedimentary unit ('E') has a more classic appearance of a syncline (Groshong, 2006) than package 'C.' Growth strata can be seen expanding landwards into the trough of the syncline.

Sediments younger than unit 'E' show less complexity in their structure. Growth faulting can be clearly observed up to the *Discorbis* 12 horizon, but the sedimentary packages between the dated horizons show little or no rotation. The horizons above *Discorbis* 12 are more or less continuous (Fig. 2).

The Corsair Growth Fault System

The Corsair growth faults in our study area appear to detach to anticlinal shale masses ('D' and 'F' in Figures 2 and 6B) and then continue downdip beyond the extent of data coverage. Similar to the shale ridge D, anticlinal feature F shows high gammy ray values and low P-wave velocity values. Its top is vaguely defined due to lack of strong reflections delineating it. The faults of the Corsair system detach to the basinward flanks of these two shale ridges. This structural setting is very similar to Bandshaw and Watkins (1994) observed in the northeast extension of the Corsair system. Shale ridge F trends parallel to the Corsair faults and seem to connect to shale ridge D at the southwestern end of our study area (Fig. 7).

A relatively thick package of sub-parellel reflections ('G' in Figures 2 and 6B) directly overlies shale ridge F on the hanging-wall of the primary Corsair growth fault. It is a landward-tilting growth package and the slope angle of the lowermost strata reach as high as 25° (Fig. 2). A series of near horizontal reflections ('H' in Figure 2) onlap against the top of package G.

Sediments younger than unit 'H' show graben faults above shale ridges 'D' and 'F.' These faults collectively cut through all the 6 chronostratigraphic horizons we have identified (Fig. 2), even though offsets across the faults are small compared to the faulting in deeper sediments.


4200 ms

5 mi

8 km

N

Primary Corsair

Shale Ridges
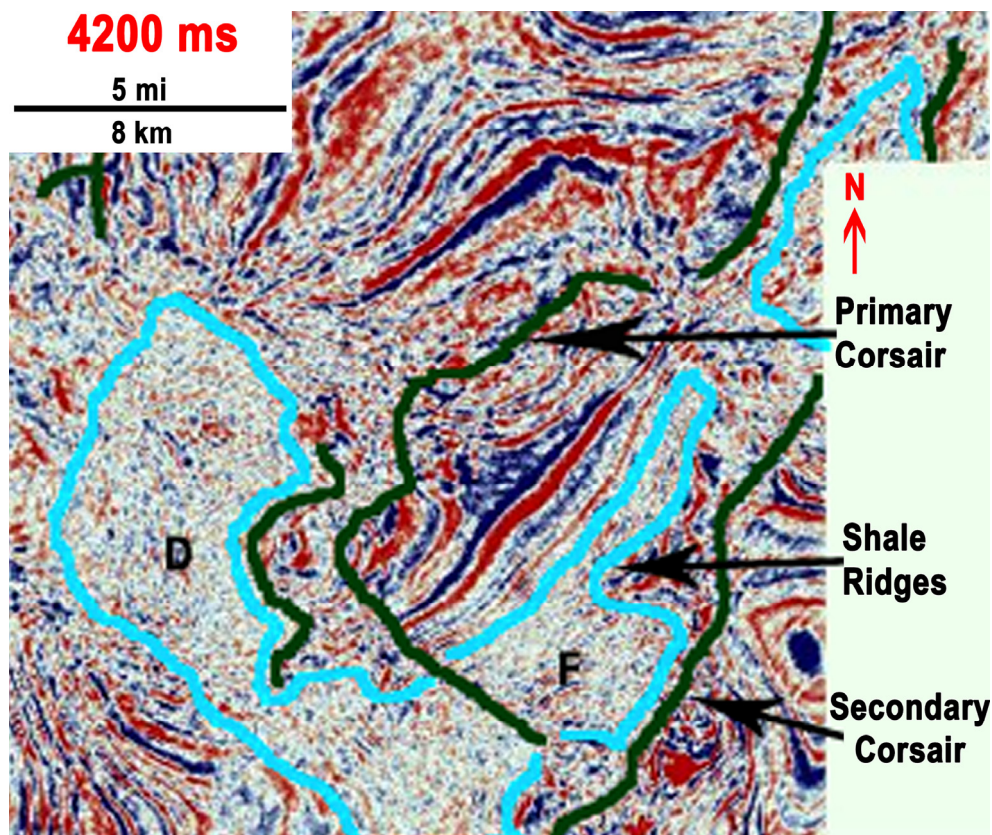
Secondary Corsair

Figure 7. Time slice at 4200 ms showing shale ridges (D and F). Shale ridge (F) trends parallel to the secondary Corsair growth faults and connects to another ridge (D) at the southwestern end of the time slice.

DISCUSSION AND CONCLUSIONS

Here we discuss the structural evolution of the sediments in the study area in two stages. The first is the succession of Clemente-Tomas and Corsair growth faulting, which took place in the early Miocene, or possibly earlier. The second stage is the early-middle Miocene through the Pliocene, which represents a period of relative quiescence with the individual faults of the systems reactivating episodically.

Growth Faulting

Previous studies (e.g., Bradshaw and Watkins, 1994; Watkins et al., 1996) conducted for the segment of the Clemente-Tomas system northeast of our study area suggest shale diapirism (e.g., Rubey and Hubbert, 1959; Daily, 1976; Galloway and Jackson, 1984) playing a primary role in its structural evolution. They further suggest that a single shale horizon forms the mobile substrate and detachment that connect the Lunker and the Clemente-Tomas systems and extend downslope beneath the Brazos ridge under the Corsair hanging wall. While many other previous studies suggest that the Corsair fault system formed as a result of salt withdrawal (e.g., Warral and Snelson, 1989; Diegel et al., 1995), some argue that the northeast Texas segment of the Corsair faults detaches onto a geopressured shale evacuation system much like the one for the Clemente-Tomas (Bradshaw and Watkins, 1994; Watkins et al., 1996). There is some similarity in the two growth fault systems between our study area and their northeast Texas segments.

Landward-dipping sedimentary units 'B' and 'E' conformably overly shale masses 'A' and 'D' (Figs. 2 and 6B). Each of B and E shows landward thickening of the strata, away from the crest of the underlying shale mass, indicating that they are growth packages. Their growth resulted from movement of the Clemente-Tomas growth faults that were accompanied by basinward rotation of the hanging wall blocks, as the shale substrate evacuated further downslope. That led to a rise of another shale anticline downslope, steepening of its overlying strata, faulting along the basinward flank of the anticline, and rotational movement of its hanging wall. Each shale-cored anticline served as a nucleus to the formation of a subsequent growth fault downslope.

Because of lack of dated chronostratigraphic horizons at the depths of units 'B' and 'E,' we cannot constrain the exact timing of these faulting events. We believe that initiation of the primary Clemente-Tomas fault significantly predated the *Marginulina* A horizon (late-early Miocene), because there exists a substantial thickness of sediments, equivalent of ~2 s TWTT, between unit 'B' and the *Marginulina* A horizon. Fault movement was probably episodic, as suggested by the downlapping in package 'C' (Fig. 2). Pauses in fault movement allowed subsequent sedimentation to reestablish near horizontal surfaces.

The Corsair growth faults within our study area detach onto the basinward flanks of the shale-cored anticlines 'D' and 'F' (Figs. 2 and 6B) and their toes continue beyond the seismic data coverage. Sedimentary unit 'G' overlying the landward slope of 'F' is another growth package. As shale ridge 'F' formed by separating itself from the older ridge 'D,' unit 'G' slid down along the basinward slope of 'D,' rotated, and helped the basinward evacuation of the underlying shale mass. Shale ridge 'F' is probably an equivalent of the Brazos Ridge (Bradshaw and Watkins, 1994). It is not certain whether or not the two are continuous, though ridge 'F' does trend along the strike of the Corsair system. Unlike the downlapping sequence observed in sedimentary unit 'C' in the Clemente-Tomas fault system, package

'H' is near horizontal and onlaps the steeply dipping unit 'G' in the Corsair fault system (Fig. 2). Continuity of the reflections within package 'H' suggests that it has experienced little to no deformation for a significant duration.

Relative Stability and Episodic Reactivation

The continuity of the *Bigenerina humblei* time horizon (13.4 Ma) and the horizons above it implies that movement of the two growth fault systems have slowed down by the middle Miocene (Fig. 2). Sedimentation in the Texas shelf slowed down considerably by the late Miocene as depocenters focused more on the Louisiana and Mississippi shelf (e.g., Galloway et al., 1991). The regional structure framework of the fault systems has not changed much since that time. Graben faults cut through these relatively young sediments and coincide with the crests of the deep shale anticlines 'A,' 'D,' and 'F,' and thus are probably associated with the diapiric movements of these shale masses. The *Bigenerina ascensionensis* (8 Ma) and *Buliminella* 1 (3.8 Ma) horizons show no obvious discontinuity within the Clemente-Tomas fault zone, while they do in the Corsair fault zone (Fig. 2). The isopach map for the *Bigenerina* A–*Discorbis* 12 interval (Fig. 5D) shows only gradual change in its thickness in the Clemente-Tomas zone, while it shows obvious change in thickness across some of the Corsair faults. This implies that the last major movement of the Corsair system occurred in the Pliocene, while Clemente-Tomas system has been inactive for a longer period.

REFERENCES CITED

Bebout, D. G., and D. R. Gutierrez, 1981, Geopressured geothermal resource in Texas and Louisiana—Geological constraints: 5th Conference, Geopressured-Geothermal Energy, Louisiana Geological Survey, Baton Rouge, Louisiana, p. 13–24.

Bradshaw, B. E., and J. S. Watkins, 1994, Growth fault evolution in offshore Texas: Gulf Coast Association of Geological Societies Transactions, v. 44, p. 103–110.

Blackwell, D., and M. Richards, 2004, Geothermal map of North America: American Association of Petroleum Geologists, scale 1:6,500,000, 1 sheet.

Dailly, G. C., 1976., A possible mechanism relating progradation, growth faulting, clay diapirism and overthrusting in a regressive sequence of sediments: Bulletin of Canadian Petroleum Geology, v. 24, p. 92–116.

Diegel, F. A., J. F. Karlo, D. C. Schuster, R. C. Shoup, and P. R. Tauvers, 1995, Cenozoic structural evolution and tectonostrati-

graphic framework of the northern Gulf Coast continental margin, *in* M. P. A. Jackson, D. G. Roberts, and S. Snelson, eds., Salt tectonics: A global perspective: American Association of Petroleum Geologists Memoir 65, Tulsa, Oklahoma, p. 109–151.

Ewing, T. E., 1983, Growth faults and salt tectonics in the Houston diaper province; relative timing and exploration significance: Gulf Coast Association of Geological Societies Transactions, v. 33, p. 83–90.

Ewing, T. H., 1991, Structural framework, *in* A. Salvador, ed., The geology of North America, v. J: The Gulf of Mexico basin: Geological Society of America, Boulder, Colorado, p. 31–52.

Ewing, T. H., and R. F. Lopez, 1991, Principal structural features, Gulf of Mexico basin, *in* A. Salvador, ed., The geology of North America, v. J: The Gulf of Mexico basin: Geological Society of America, Boulder, Colorado, plate 2, scale 1:2,500,000.

Galloway, W. E., D. G. Bebout, W. L. Fisher, J. B. Dunlap Jr., R. Cabrera-Castro, J. E. Lugo-Rivera, and T. M. Scott, 1991, Cenozoic, *in* A. Salvador, ed., The geology of North America, v. J: The Gulf of Mexico basin: Geological Society of America, Boulder, Colorado, v. J, p. 245–324.

Griggs, J., 2005, A reevaluation of geopressured-geothermal aquifers as an energy source: 13th Workshop on Geothermal Reservoir Engineering, Stanford University, California, p. SGP–TR–176.

Groshong, R. H., Jr., 2006, 3-D structural geology—A practical guide to quantitative surface and subsurface map interpretation, 2nd ed.: Springer, New York, New York, p. 89–106.

Huh, S., 1995, Structure and seismic stratigraphy of the Brazos, Galveston, and High Island OCS area, Gulf of Mexico and Palinspastic reconstruction of the Corsair fault: Ph.D. Dissertation, Texas A&M University, College Station, 259 p.

Huh, S., J. S. Watkins, R. Kasande, J. C. Fiduk, S. Bryant, K. E. Silver, B. E. Bradshaw, F. Xue, and J. Xi, 1996, Regional structure and tectonics of the Texas shelf: Gulf Coast Association of Geological Societies, p. 39–51.

Kasande, R., 1995, Miocene structure of Mustang Island, Mustang Island East Addition and part of Matagorda Islands, outer continental shelf areas, Gulf of Mexico: M.S. Thesis, Texas A&M University, p. 69.

Lam, N. S., 1983, Spatial interpolation methods review: The American Cartographer 10: p. 129–149.

McDonnell, A., M. R. Hudec, and M. P. A. Jackson, 2009, Distinguishing salt welds from shale detachments on the inner Texas shelf, western Gulf of Mexico: Basin Research, v. 21, p. 47–59, doi:10.1111/j.1365-2117.2008.00375.x.

McDonnell, A., M. P. A. Jackson, and M. R. Hudec, 2010, Origin of transverse folds in an extensional growth-fault setting: Evidence from an extensive seismic volume in the western Gulf of Mexico: Marine and Petroleum Geology, v. 27, p. 1494–1507.

McKenna, T. E., 1997, Fluid flow and heat transfer in overpressured sediments of the Rio Grande embayment, Gulf of Mexico basin: Gulf Coast Association of Geological Societies Transactions, v. 47, p. 351–366.

McKenna, T. E., and J. M. Sharp, 1997, Subsurface temperatures, fluid pressures, and salinities in the Rio Grande embayment, Gulf of Mexico basin, U.S.A.: 30th International Geological Congress, Beijing, China, p. 263–274.

Morton, R. A., L. A. Jirik, and R. Q. Foote, 1985, Depositional history, facies analysis and production characteristics of hydrocarbon bearing sediments, offshore Texas: Texas Bureau of Economic Geology Geological Circular 85–2, Austin, 31 p.

Morton, R. A., L. A. Jirik, and W. E. Galloway, 1988, Middle-upper Miocene depositional sequences of the Texas coastal plain and continental shelf: Geologic framework, sedimentary facies, and hydrocarbon plays: Texas Bureau of Economic Geology Report of Investigations 174, Austin, 40 p.

Nagihara, S., 2010, Characterization of the sedimentary thermal regime along the Corsair growth-fault zone, Texas continental shelf, using corrected bottom hole temperatures: American Association of Petroleum Geologists Bulletin, v. 94, p. 923–935, doi:10.1306/01051009092.

Nagihara, S., and M. A. Smith, 2008, Regional overview of deep sedimentary thermal gradient of the geopressured zone of the Texas-Louisiana continental shelf: American Association of Petroleum Geologists Bulletin, v. 92, p. 1–14, doi:10.1306/08070706111.

Rubey, W. W., and M. K. Hubbert, 1959, Role of fluid pressure in mechanics of overthrust faulting: II. Overthrust belt in geosynclines area of western Wyoming in light of fluid pressure hypothesis: Geological Society of America Bulletin, v. 70, 167–205.

Sheriff, R. E., and L. P. Geldart, 1995, Exploration seismology, 2nd ed.: Cambridge University Press, New York, New York, 623 p.

Stanley, T. B., Jr., 1970, Vicksburg fault zone, Texas, *in* M. T. Halbouty, ed., Geology of giant petroleum fields: American Association of Petroleum Geologists Memoir 14, Tulsa, Oklahoma, p. 301–308.

Taylor, T. R., and L. S. Land, 1996, Association of allochthonous waters and reservoir enhancement in deeply buried Miocene sandstones: Picaroon field, Corsair trend, offshore Texas, *in* L. J. Crossey, R. Loucks, and M. W. Totten, eds., Siliciclastic digenesis and fluid flow: Concepts and applications: Society of Economic Paleontologists and Mineralogists Special Publication 55, Tulsa, Oklahoma, p. 37–48.

Watkins, J. S., B. E. Bradshaw, S. Huh, R. Li, and J. Zhang, 1996a, Structure and distribution of growth faults in the northern Gulf of Mexico OCS, *in* J. O. Jones and R. L. Freed, eds., Structural framework of the northern Gulf of Mexico: Gulf Coast Association of Geological Societies, Austin, Texas, p. 63–77.

Weber, D., and E. Englund. 1994. Evaluation and comparison of spatial interpolators II: Mathematical Geology, v. 26, p. 589–603.

Witrock, R. B., A. R. Friedmann, J. J. Galluzzo, L. D. Nixon, P. J. Post, and K. M. Ross, 2003, Biostratigraphic chart of the Gulf of Mexico offshore region, Jurassic to Quaternary, U.S. Department of the Interior, Minerals Management Service, New Orleans, Louisiana.